



# A Validation Methodology for Urea Spray on Selective Catalytic Reduction Systems

İsmail Hakkı Savcı<sup>1</sup>, Mehmet Zafer Gül<sup>2</sup>, Ramazan Şener<sup>3,\*</sup>

<sup>1</sup> Ford Otosan Company, Product Development Department, 34885, Istanbul, Turkey.

<sup>2</sup> Department of Mechanical Engineering, Marmara University, 34722, İstanbul, Turkey.

<sup>3</sup> Department of Electronics and Automation, Batman University, 72100, Batman, Turkey.

## Abstract

Selective catalytic reduction (SCR) is an emission control method that reduces the NO<sub>x</sub> emission using urea sprays as ammonia precursors for exhaust after-treatment systems. The urea injection system is an essential component of the SCR systems. A comprehensive SCR modeling approach is required to design compact after-treatment systems that meet the NO<sub>x</sub> emission legislation level. In this study, the characteristics of urea spray injectors of the SCR system were investigated using computational fluid dynamics (CFD) and the particle image velocimetry (PIV) technique. A validation strategy was developed to model the urea spray evaporation, liquid/wall contact, and formation of solid urea deposits. The sheet atomization model was modified to improve the performance of the CFD model. While the Rosin-rammler method predicted the results of 10% according to the experimental results, the proposed tabular method decreased the difference by 3%. In addition, 500 parcels were determined as an optimum number of parcels for urea spray according to the sensitivity study. Therefore, the validation methodology was proposed to predict more consistent results for urea spray modeling and the formation of solid urea deposits.

**Keywords:** Selective catalytic reduction; Urea Spray; CFD; PIV; Visualization.

## 1. Main text

In the past decades, diesel engines have been the dominant power source for medium and heavy-duty commercial vehicle applications such as trucks, buses, and off-road vehicles. Diesel engines are also commonly used for light-duty applications such as passenger cars [1, 2]. The main advantages of diesel engines are increased fuel economy, higher durability, increased torque, and low taxes imposed by the government compared to a similar engine displacement of a gasoline engine. The main disadvantages of diesel engines are harmful exhaust gases due to the diesel combustion process [3]. These exhaust emissions threaten public health with three primary pollutants [4]. First, particulate matters (PM) are a complex mixture generated from diesel combustion. PM is made up of hundreds of chemicals adsorbed which are mostly carcinogens. The small particulate matter size, around 1-2µm, directly affects public health, particularly for the lung [5]. Carbon monoxide (CO) is a toxic chemical. It is produced from partial combustion [6].

\* Corresponding author. Tel.: +90-488-217-3500; fax: +90-488-217-3500.

E-mail address: ramazan.sener@batman.edu.tr

Nitrogen Oxide ( $\text{NO}_x$ ) is produced from the combustion of nitrogen at high temperatures [7, 8].  $\text{NO}_x$  can form a nitric acid vapor. Nitric acid vapor can penetrate and damage the lungs [9]. These three emissions should be removed from the environment due to their hazardous effect on public health. Stringent legislative emission standards to protect public health for heavy diesel duty and light duty engines were introduced by European Commission, the United States, and China government commissions. Fig. 1 presents the significant reduction of PM and  $\text{NO}_x$  for heavy-duty vehicles. These reductions show the reduction progression from 1992 to 2015 [10]. The standards are defined by the vehicles' energy output ( $\text{g/kwh}$ ). The emission standards are based on a test cycle that represents the real driving style of the drivers. Each standard emission shapes Euro 3, Euro 4, Euro 5, Euro 6, and Euro 7 represents the rectangular. Using the Euro 6 strategy with exhaust gas recirculation (EGR) and selective catalytic reduction (SCR) may require a diesel particulate filter (DPF) to meet the Euro 6 emission standard for the PM [11].

The current strategies attempting to minimize fuel consumption, standalone SCR, and DPF might be sufficient to meet the Euro VI standard. However, an advanced strategy is required to optimize the urea injection strategy and fuel consumption without EGR hardware, leading to a high emission reduction of  $\text{NO}_x$ . SCR may be more advantageous, especially in the heavy-duty truck application, than the competing EGR technology, which brings a fuel economy penalty [12]. However, one must remember that SCR engines' fuel savings are at least partially offset by the cost of urea, which is consumed at about 3-5% of the fuel volume [13]. Therefore, this method results in a better fuel economy without additional hardware. The challenging part of this strategy is high  $\text{NO}_x$  reduction in the exhaust after treatment. Thus, optimized SCR system design and urea injection calibration are critical to achieving this strategy [14].

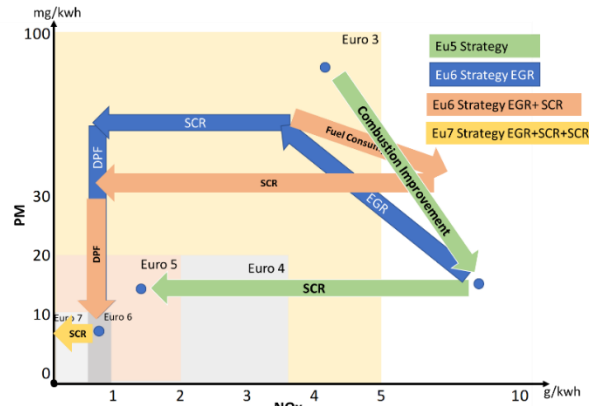


Fig 1: Improvement of Emission Reduction by using different strategies

The SCR system with ammonia ( $\text{NH}_3$ ) injection in automotive applications is a widely used emission reduction technique to convert the  $\text{NO}_x$  emissions to nitrogen and water [15]. However, pure ammonia is a toxic reducing agent for mobile applications [16]. Urea Water Solution (UWS) has transport and storage advantages over ammonia [17]. Urea should decompose to ammonia and carbon dioxide over SCR with  $\text{NH}_3$  process with a lower conversion ratio [18]. Numerous numerical studies were used in the literature [19, 20]. CFD code based on the finite volume method was implemented in this study.

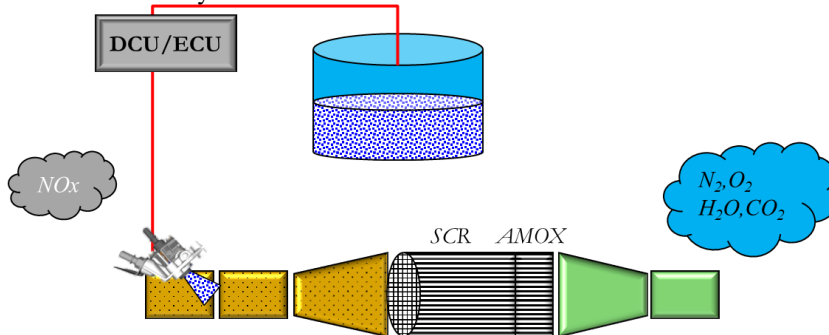


Fig 2: Selective catalytic reduction system

The major components of the active SCR system are a dosing module, SCR catalyst,  $\text{NO}_x$ , and temperature sensor. The dosing module controls the mass flow rate of the urea-water solution. The honeycomb SCR catalyst accelerates a chemical reaction, and  $\text{NO}_x$  and sensors measure the gas temperature [21].

A comprehensive SCR modeling approach is required to design compact after-treatment systems that meet the  $\text{NO}_x$  emission legislation level. In this work, the sheet atomization model was implemented in Star-CCM+. Some modifications were made to determine initial spray parameters and velocity over the original model. Simulations were carried out to model sprays measured in a spray test bench to assess the model's capability. One case from the literature was studied with a correlated spray model. The simulation results were compared with spray images obtained from literature images. A reasonably good agreement between simulation and experiment was obtained. The spray modeling, results of the optical spray setup, and their comparison are discussed in this paper. Urea spray distribution on the SCR inlet is the most critical parameter for SCR performance. So robust urea spray CFD methodology is the main part of the complex SCR CFD modeling approaches [22, 23]. Detailed chemistry and flow modeling techniques should be based on urea spray modeling.

## 2. Material and Methods

### 2.1. Experimental Bench

The most used experimental techniques for spray characterization of urea injectors are Phase Doppler Particle Analyzer and Particle Image Velocimetry (PIV). However, Phase Doppler Analyzer was not available for this study. PIV and shadow imaging systems (Particle Master) were used to examine spray characterization such as cone angle, spray range, spray distribution, drop size, and velocity data of spray across the laser sheet area. Droplets' Sauter mean diameter (SMD) was measured using the shadowgraph technique with the long-distance microscope [24].

PIV is an application of the laser sheet technique. A laser sheet is a double pulsed laser sheet in a brief time interval. The laser sheet is pulsed twice, and a CCD camera can capture illustrated regions—these techniques are based on the Lagrangian approach. The positions of the particles are tracked for calculations. The first laser sheet illustrates these droplets' initial positions, and the camera captures these frozen images. Then droplets are advanced, and the second image of the camera is exposed to the light scattered by the particles from the second laser pulse. Hence two images are collected; the first image shows the first position of the particles, and the second picture shows the advanced position. The velocity vector is calculated by measuring the particle displacement at a particular time [25]. PIV technique can also be used with several exposed frames strategy, and each particle is moved in several times to different locations on the same picture. PIV performs an average of the velocity field vector. Autocorrelation or cross-correlation functions are post-processed between two images. This technique has the advantage, is not being biased by the gradient since the individual particles are tracked individually to get a velocity vector [25, 26].

The schematic in Fig. 3 shows the experimental configuration for the laser PIV and shadowgraph for the particle master experiment. The test bench was designed and developed with a laser, camera, led light, and injection module synchronization unit. For these experiments, laser sheets (2mm) were introduced through the spray. The imaging system was composed of a camera and laser light source. The cameras were a Lavision Flowmaster digital CCD device with a pixel resolution of 1280 columns and 1024 rows with a 12-bit dynamic range and Phantom high-speed camera. A 532 nm bandpass filter was used with a 50 mm f/2.8 Nikon camera lens. The laser was the double pulse; frequency-doubled nd: YAG laser. Typical pulse durations for the imaging experiments were 1 mJ/5-7 ns at 532 nm, and the laser has a maximum repetition rate of 15 Hz. Particle Master System includes Led light, a laser with an ultra-short pulse.

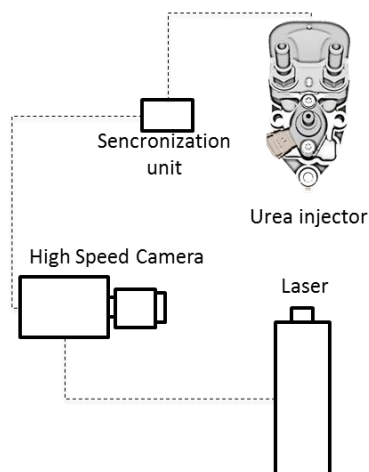
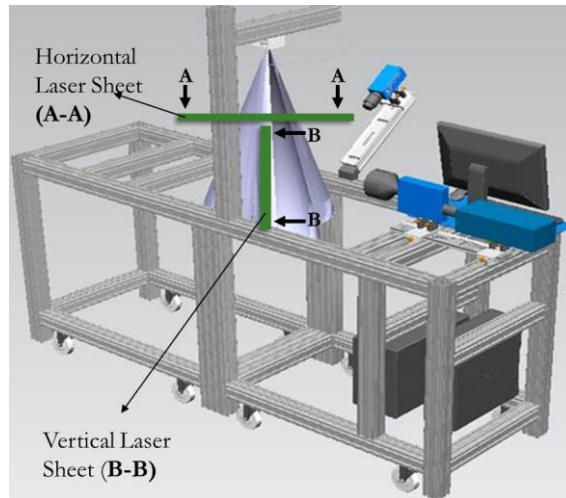


Fig 3: A simple schematic view of PIV

The optical urea spray experimental setup is shown in Fig. 4. The setup was designed for injector testing and modified for optical measurements. In addition, the experimental setup was arranged for parallel and horizontal sectional spray measurements.

A horizontal spray measurement was used to characterize the spray distribution, such as spray cone angle. Second, the spray balance was visualized by vertical measurement from each injector hole. Finally, the particle master measured the spray size. Thus, one test rig was designed for three different purposes.

A Xenon lamp was used as a light source for the spray distribution, and a high-speed camera was used to capture the spray image. First, the spray behavior was visualized on a laser sheet using a YAG laser and optical arm. This visualization result qualitatively confirmed the spray's cross-sectional pattern and mass flux distribution because the intensity of the scattered light relied on the droplet density and diameter. The first injector spray distribution was observed in Fig. 5. Next, the spray angle, penetration length, and penetration length were extracted from laser measurement.



**Fig 4: The optical spray experimental setup**

The spray distribution through the surface normal of the nozzle is visualized to check spray balance from each injector hole (six holes injectors) and for injector quality testing. Each nozzle was not discharged with the same amount of urea as the first injector. Therefore, a problem was detected with the first injector. A new injector based on the correct specification was ordered and used in this work. For each urea injector characterization test, injectors should measure from the surface normal of the injector hole to observe the urea balance from each injector hole (three holes injectors).

In the experimental spray calibration process, droplet distribution was measured 100 mm below the injector tip through the spray. This data was then proceeded to calculate the SMD over the beam. The spray angle was measured by the intersection of the spray's two outside edges at the nozzle. There were injection-to-injection variations due to injector pumps. Therefore, the spray cone angles varied from  $33^\circ$  to  $48^\circ$ . Five individual measurements were done to eliminate this noise factor, and average data was extracted for post-processing. The spray angle was again determined to be  $33^\circ$ . After sampling many instantaneous images, an average spray particle diameter distribution was determined in Fig. 8.

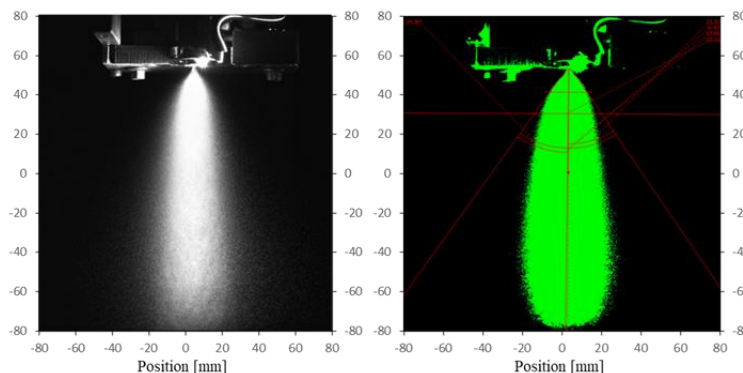


**Fig 5: Spray distribution**

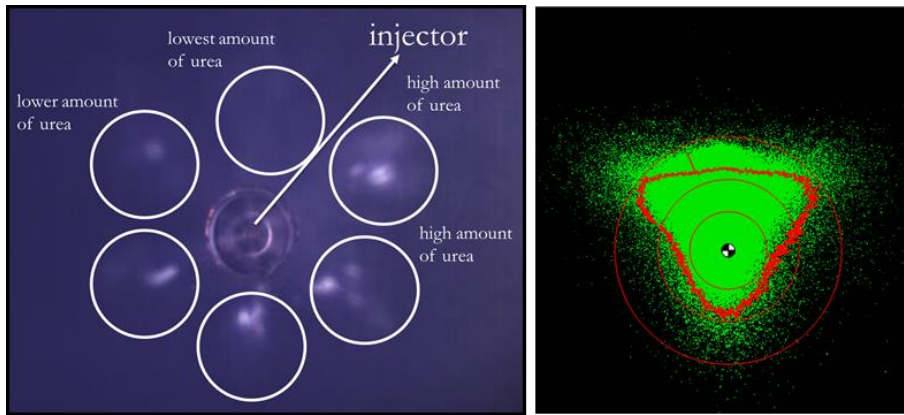


Fig 6: Spray distribution seeing from the surface normal a) unbalanced spray distribution b) balanced spray distribution

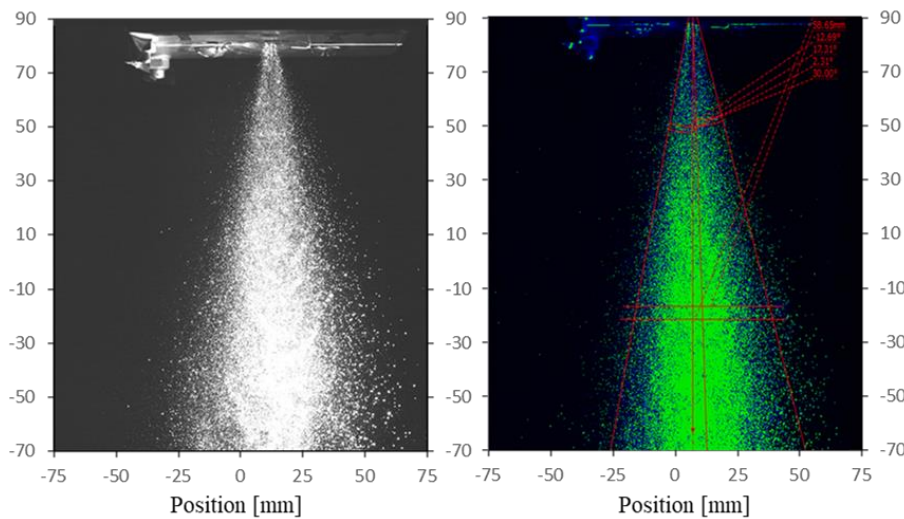


Fig 7: Spray distribution

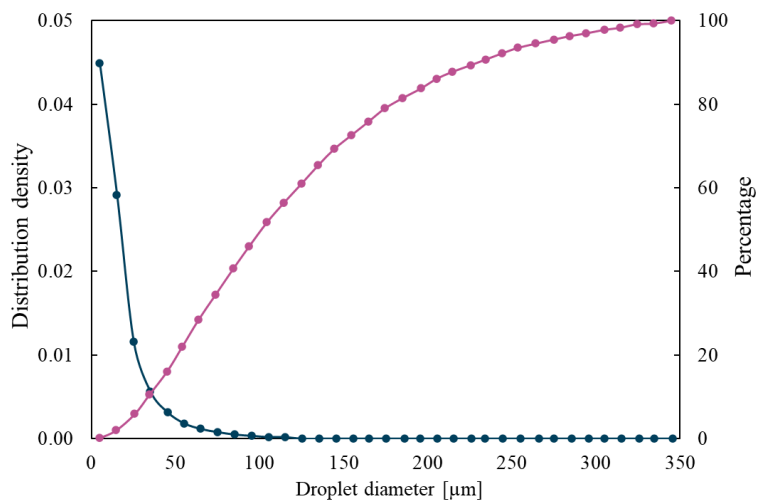


Fig 8: Droplet diameter distribution

2.2. Spray Modelling

First, a free spray was simulated to match the measured droplet size and velocity at the center point 100 mm downstream. Then, the results were shown as measured data for the average of five individual experiments.

Although initial droplet sizes were used at the injector tip in the simulations, even these values were extracted 100 mm downstream of the injector tip. Therefore, this calibration study was performed to eliminate this assumption. So initial droplet size was specified at the injector tip, and the droplet size was 100 mm downstream of the injector tip. If the results are not comparable, a new iteration is applied to the injector tip. For this approach, Rosin-rammler and tabulated distribution methods were examined.

The computational domain was built as the cylindrical region with dimensions of 90 mm diameter, and 115 mm height with the three-hole injector at the top center, directed in the axial direction in Fig. 9. A cylindrical chamber mesh represents the calibration chamber (also known as Glass Bomb) to tune spray parameters in the CFD model with the experimental test result. Local refinement was applied to the tips of the nozzle to improve resolution. Boundaries were set to pressure boundaries. Because the size of the domain was sufficiently large, pressure boundaries monitored the droplets, and there were no droplets that had passed through boundaries. Since the test was usually carried out with the injector pointing toward the ground, the gravity should be set in the same direction.

Air in the cylindrical domain was modeled as an ideal gas. The standard k- $\epsilon$  model was employed. The energy equation was not solved. All the walls of the cylindrical domain were modeled with free slip conditions. The flow was assumed to be stagnant to begin. This section describes the modeling approach based on StarCCM+. The mesh sensitivity has been evaluated on mass transfer. The global mesh size was 1 mm, but the mesh size of the spray zone was specified at 0.5 mm. The double number of mesh did not affect the mass transfer, so current settings were kept for this simulation study.

High-speed shadowgraph images of the one spray injection in ambient conditions highlight its structures. The three-hole injector produced three distinct jets of fluid with long breakup lengths. A three-hole injector could not produce a uniform distribution of spray across its cross-section. It has been found that the atomization of the spray from the injector is consistent for each dosing event. Only injection starting internal time the spray oscillation was observed. 200 mg/s, 500 mg/s, and 1000 mg/s have been experimented with, and the dosing rate does not affect spray distribution.

$$Q = 1 - \exp\left[-\left(\frac{D}{D_{ref}}\right)^q\right] \quad (1)$$

The volume distribution of particles as a function of their diameter can be obtained from equation 1. It is easy to calibrate since it has only two variables. However, if the measured value was specified at the injection tip, a 30% error was obtained 100 mm downstream of the injector type. The diameter distribution for the injected droplets was given by a Rosin-rammler function as specified in Fig. 10. Parameters of the Rosin-rammler were modified and set three can predict a 10% error with the experiments.

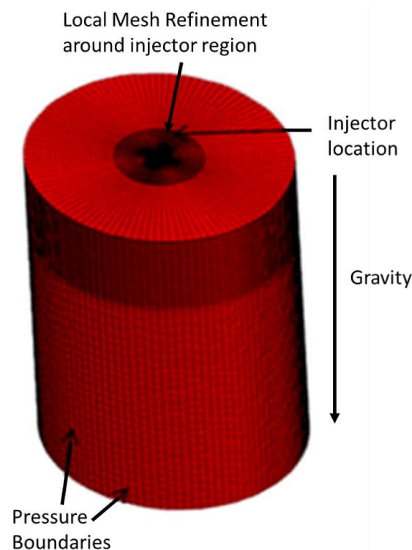


**Fig 9: The computational grid**

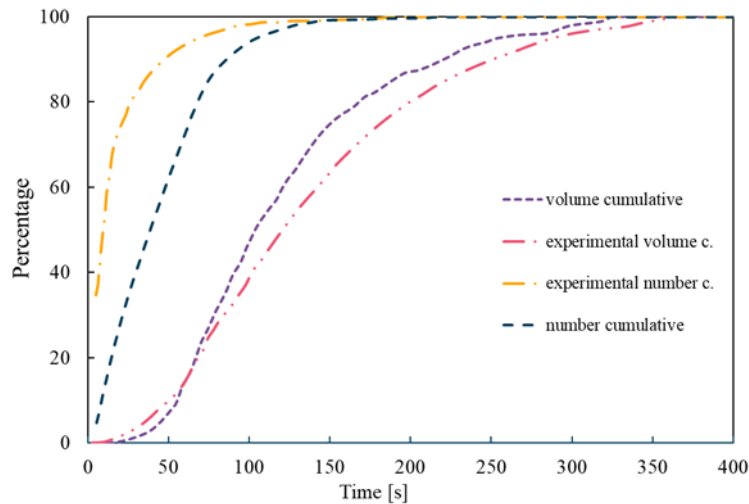


Fig 10: Rosin-rammler iterative method

Table approach, the droplet distribution, e.g., from measurement, was used as the initial guess. The correlation was around 10% error at the first attempt. Finally, the droplet diameter tabulated is modified to further Star-CCM+ calculation and predict correlation well with experiment data.

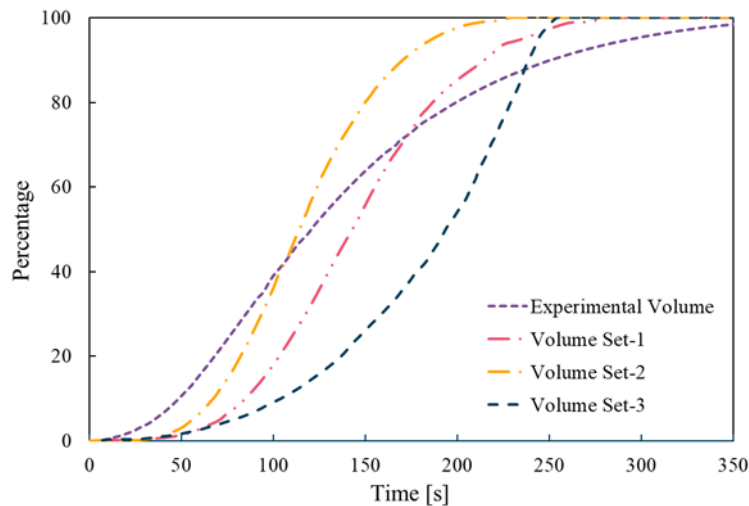


Fig 11: Droplet table method for droplet diameter

Experimental data on the lateral plane was compared with numerical data on the corresponding plane to arrive at better empirical model constants in Fig. 12. The spray structure was defined in Fig. 12. Droplet diameters were extracted using the CFD and compared with the results of the PIV test (Table 1). The correlation has seemed well with the experimental result.

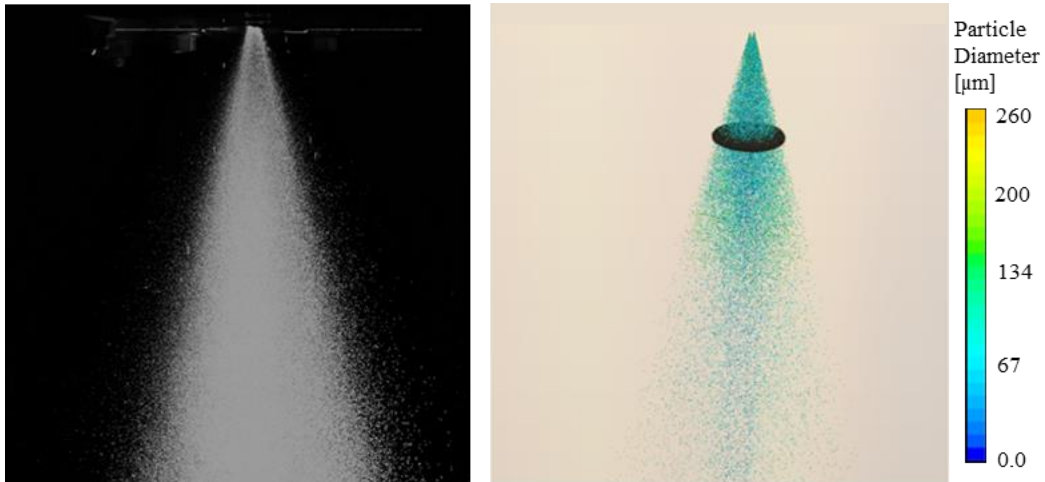


Fig 12: Comparison of experimental and computed spray distribution

Table 1: Injector specifications

Injector A	Spray Angle	Penetration Length
Test Results	33	38
CFD results	32	36

### 3. Results and Discussion

The glass windows installed test pipe was modeled as three-dimensional for CFD analysis to investigate spray/wall interaction and deposit accumulation [27]. A steel plate, injector, and glass windows were considered, which is shown in Fig. 13. The CFD model was generated with polyhedral mesh from StarCCM+. Local mesh refinement was generated around the injector and spray path. The entire model consists of 3.5 million cells, with mainly 1.2 million boundary layer cells. At the injection region, the base cell was 1 mm. region of the injector and regions of the spray path were refined with the base cell size of 0.5 mm. The thickness of the wall layer varies from 0.5 to 1.5 mm. This layer was essential for the high result quality of the HTC [28]. CFD parameters used in this study are listed in Table 2.

Table 2: CFD settings

Flow Characteristics	Compressible, Turbulent, Time-dependent
CFD Solver	Star-CCM+
Turbulence Model	Standard k- $\epsilon$ with wall function
Solution Algorithm	Simple, double precision
Residual levels	<0.0001

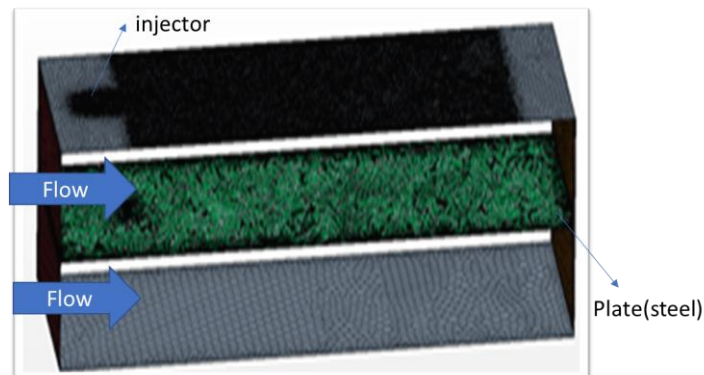


Fig 13: Sketch the experimental setup for spray/wall interaction

Fig. 14 shows the spray pattern at 4 ms, 10ms, and 20ms a side view of the measured spray penetration at different times with the shadowgraph method [27].

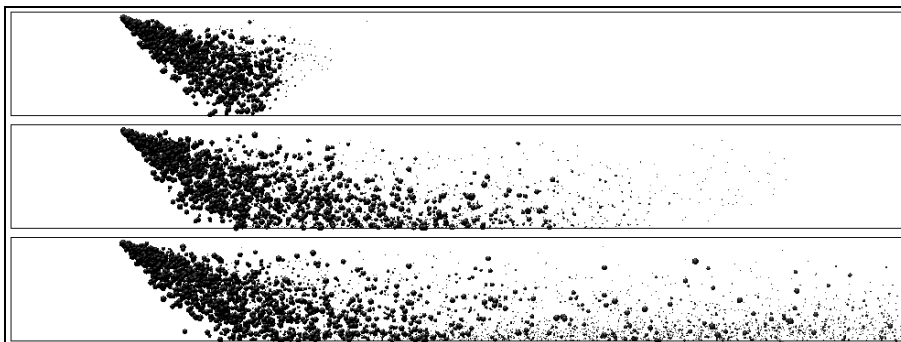


Fig 14: Spray pattern at 4 ms, 10 ms, and 20 ms [25]

Fig. 15 shows the numerical result of defined geometry in Star-CCM+. The results were compared with the test result. This model predicted tiny droplets due to thermal breakup. Penetration length and spray cone angles were similar in both simulation and experiment. Therefore, only tiny droplets could not be captured by the CFD. The predicted wall film thickness in Fig. 16 reflects spray character with the film thickness in the spray impact region. These wall film characteristics correlate with visual observations during the experiment.

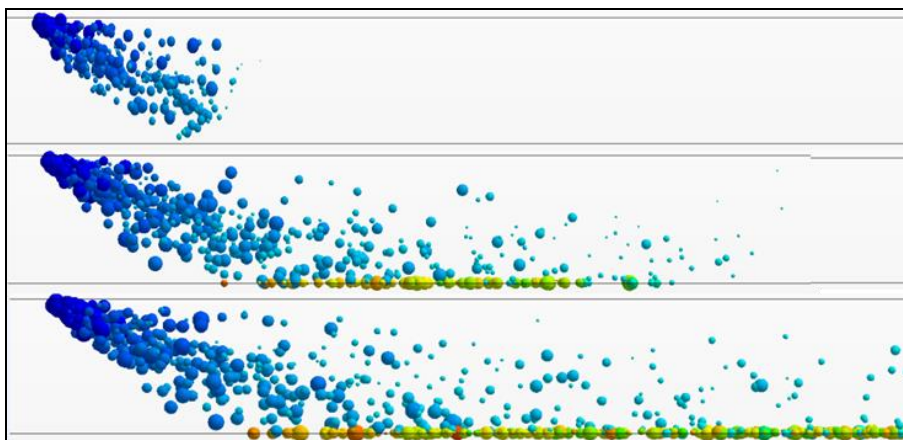


Fig 15: The spray pattern of numerical models at 4 ms, 10 ms, and 20 ms

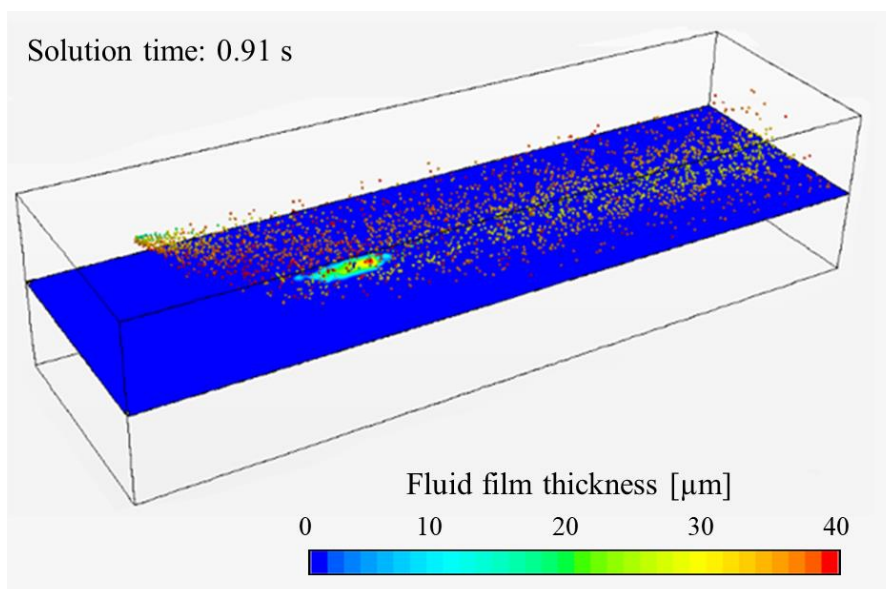


Fig 16: Predicted wall film thickness with spray distribution

Fig. 17 shows the urea concentration in the wall film. In the spray impact region, the urea concentration occurred by the urea fraction of the droplets. Due to the evaporation of water from urea concentration, droplets increased significantly. As the wall film was moved downstream with minor droplet impingement, higher urea concentrations occurred due to water evaporation. After water evaporation was completed, thermolysis of urea began in these regions. Thus, thermolysis reactions became dominant for  $\text{NH}_3$  conversion.

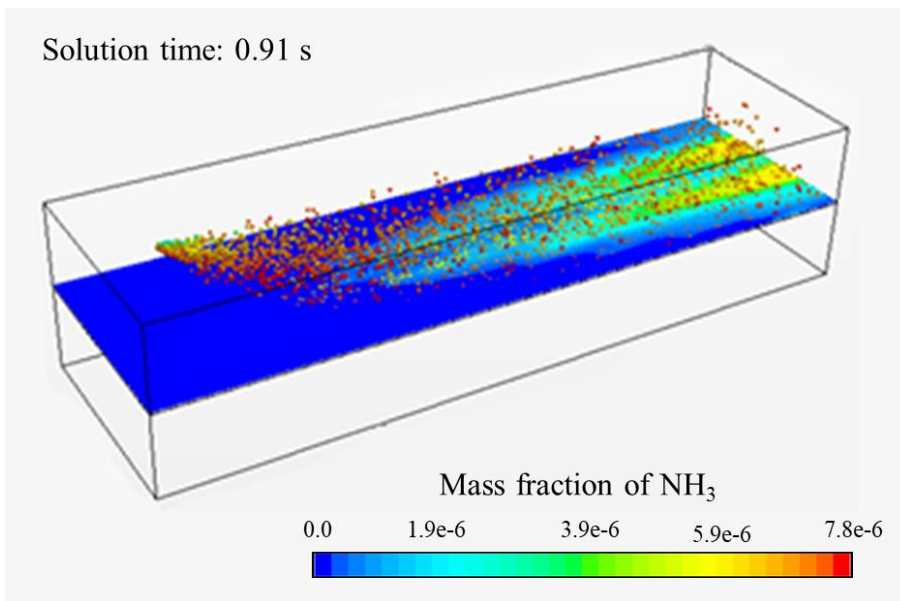


Fig 17: Calculated mass fraction of urea in the wall

Fig. 18 presents views of the ammonia at the center of the model. In the center of the model, ammonia was produced significantly higher than the other model parts. The main reason behind these results was to thermolysis reaction of tiny droplets. Ammonia generation can be observed by urea decomposition from the boundaries of the models. In addition, tiny droplets lead to evaporation and faster thermolysis, so more  $\text{NH}_3$  conversion can be observed on the surface.

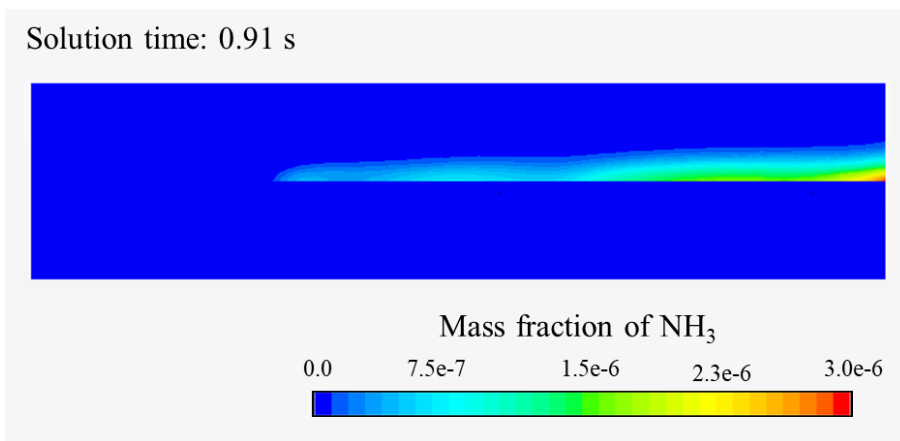


Fig 18: Calculated mass fraction urea at the lateral plane

#### 4. Conclusion

Urea spray modeling is one of the challenging steps to achieving SCR system modeling including complex interactions of multi-phase physics and chemical reactions. The characteristics of urea injectors were investigated using numerical and experimental methods. As a result of this study, the spray validation methodology was developed for urea spray on SCR systems.

- Unbalanced spray negatively affects the spray dispersion performance of the injector and increases the possibility of deposit formation. Before performing the spray and cone angle tests, the radial spray distribution of the injector should be checked.

- With the tabular method, CFD results can be estimated in good correlation with the experimental results. While the error rate was 10 percent in the solutions made with the Rosin-rammler method, it decreased by 3 percent in the tabular method.
- The spray sensitivity work was experimented with to determine the appropriate droplet parcel number. Less droplet parcels could not carry necessary information, high parcel numbers have time penalty and convergence issue. 50 to 5000 parcels are simulated then 500 parcels have been selected in spray simulations as an optimum parcel number.
- Rosin-rammler and tabular methods accelerated the simulation. In addition, the simulation results with the tabular method were more consistent with experimental results than the Rosin-rammler method.
- As a standard approach, spray data extracted from the experiment is used as direct input in simulation studies. In this study, the spray data extracted from the experiment were firstly adjusted on the CFD test bench and the distribution obtained from the CFD was used in the applications. Hence, 8 percent more accurate data is used as input to the CFD.

## Acknowledgements

The authors also would like to thank the Ford Otosan Company for providing a test and software facility.

## References

- [1] R. Şener, M. Z. Gül, Optimization of the combustion chamber geometry and injection parameters on a light-duty diesel engine for emission minimization using multi-objective genetic algorithm, *Fuel*, Vol. 304, pp. 121379, 2021.
- [2] R. Sener, M. U. Yangaz, M. Z. Gul, Effects of injection strategy and combustion chamber modification on a single-cylinder diesel engine, *Fuel*, Vol. 266, pp. 117122, 2020.
- [3] R. Şener, M. R. Özdemir, M. U. Yangaz, Influence of piston bowl geometry on combustion and emission characteristics, *Proceedings of the Institution of Mechanical Engineers, Part A: Journal of Power and Energy*, Vol. 233, No. 5, pp. 576-587, 2019.
- [4] A. Winer, W. Busby, Atmospheric transport and transformation of diesel emissions, *Diesel exhaust: A critical analysis of emissions, exposure, and health effects*, pp. 83-105, 1995.
- [5] H. Omidvarborna, A. Kumar, D.-S. Kim, Recent studies on soot modeling for diesel combustion, *Renewable and Sustainable Energy Reviews*, Vol. 48, pp. 635-647, 2015.
- [6] B. Weinstock, H. Niki, Carbon monoxide balance in nature, *Science*, Vol. 176, No. 4032, pp. 290-292, 1972.
- [7] T. Kaya, O. A. Kutlar, O. O. Taskiran, Evaluation of the partially premixed compression ignition combustion with diesel and biodiesel blended diesel at part load condition, *Engineering Science and Technology, an International Journal*, Vol. 24, No. 2, pp. 458-468, 2021.
- [8] R. Şener, Numerical Investigation of Ducted Fuel Injection Strategy for Soot Reduction in Compression Ignition Engine, *Journal of Applied Fluid Mechanics*, Vol. 15, No. 2, pp. 475-489, 2022.
- [9] D. Fowler, C. Flechard, U. Skiba, M. Coyle, J. N. Cape, The atmospheric budget of oxidized nitrogen and its role in ozone formation and deposition, *The New Phytologist*, Vol. 139, No. 1, pp. 11-23, 1998.
- [10] W. A. Majewski, Diesel particulate filters, *DieselNet, Ecopoint Inc, Brampton, ON, Canada*, 2001.
- [11] H. Steven, Development of a worldwide harmonised heavy-duty engine emissions test cycle, *Final Report, April*, 2001.
- [12] X. Li, Y. Cheng, Z. Zhang, S. Ji, The Effect of Coupling Injection Parameters and Double-Swirl Chamber on the Diesel Engine Performance, *Arabian Journal for Science and Engineering*, Vol. 44, No. 2, pp. 1393-1401, 2019.
- [13] G. Zheng, A. Kotrba, M. Golin, T. Gardner, A. Wang, *Overview of large diesel engine aftertreatment system development*, 0148-7191, SAE Technical Paper, pp. 2012.
- [14] Q. Song, G. Zhu, Model-based closed-loop control of urea SCR exhaust aftertreatment system for diesel engine, *SAE Transactions*, pp. 102-110, 2002.
- [15] R. M. Heck, Catalytic abatement of nitrogen oxides—stationary applications, *Catalysis Today*, Vol. 53, No. 4, pp. 519-523, 1999.

- [16] M. Koebel, E. O. Strutz, Thermal and hydrolytic decomposition of urea for automotive selective catalytic reduction systems: thermochemical and practical aspects, *Industrial & engineering chemistry research*, Vol. 42, No. 10, pp. 2093-2100, 2003.
- [17] Y. Itaya, NO reduction behavior by urea solution injection in the tubular reactor, in *Proceeding of*.
- [18] W. Held, A. Koenig, T. Richter, L. Puppe, Catalytic NOx reduction in net oxidizing exhaust gas, *SAE transactions*, pp. 209-216, 1990.
- [19] M. Mohammadi, M. Goodarzi, M. Ghayour, S. Alivand, Small scale effect on the vibration of orthotropic plates embedded in an elastic medium and under biaxial in-plane pre-load via nonlocal elasticity theory, 2012.
- [20] A. Farajpour, M. Mohammadi, A. Shahidi, M. Mahzoon, Axisymmetric buckling of the circular graphene sheets with the nonlocal continuum plate model, *Physica E: Low-dimensional Systems and Nanostructures*, Vol. 43, No. 10, pp. 1820-1825, 2011.
- [21] I. H. Savci, M. Z. Gul, A methodology to assess mixer performance for selective catalyst reduction application in hot air gas burner, *Alexandria Engineering Journal*, Vol. 61, No. 9, pp. 6621-6633, 2022.
- [22] W. Edelbauer, F. Birkhold, T. Rankel, Z. Pavlović, P. Kolar, Simulation of the liquid break-up at an AdBlue injector with the volume-of-fluid method followed by off-line coupled Lagrangian particle tracking, *Computers & Fluids*, Vol. 157, pp. 294-311, 2017.
- [23] N. D. Nasello, F. Gramigni, I. Nova, E. Tronconi, AdSCR Systems (Adsorption+ Selective Catalytic Reduction): Analysis of the Influence of H2O and CO2 on Low Temperature NOx Emission Reduction Performances, *Emission Control Science and Technology*, Vol. 7, No. 4, pp. 223-231, 2021.
- [24] M. Zöchbauer, H. Smith, T. Lauer, *Advanced SCR flow modeling with a validated large eddy simulation*, 0148-7191, SAE Technical Paper, pp. 2015.
- [25] LaVision. [www.lavision.de](http://www.lavision.de), Accessed.
- [26] İ. H. Savcı, R. Şener, İ. Duman, A study of signal noise reduction of the mass air flow sensor using the flow conditioner on the air induction system of heavy-duty truck, *Flow Measurement and Instrumentation*, Vol. 83, pp. 102121, 2022.
- [27] F. Birkhold, U. Meingast, P. Wassermann, O. Deutschmann, Analysis of the injection of urea-water-solution for automotive SCR DeNOx-systems: modeling of two-phase flow and spray/wall-interaction, *SAE Transactions*, pp. 252-262, 2006.
- [28] I. Savci, *An Integrated Modeling Approach to Investigate Performance of Selective Catalyst Reduction*, Thesis, PhD Thesis, University of Marmara, 2015.